

Tunable atomically enhanced moiré Berry curvatures in twisted triple bilayer graphene

Konstantin Davydov¹, Ziyang Zhu², Noah Friedman¹, Ethan Gramowski¹, Yaotian Li¹, Jack Tavakley¹, Kenji Watanabe³, Takashi Taniguchi⁴, Mitchell Luskin⁵, Efthimios Kaxiras^{6,7}, Ke Wang^{1*}

¹*School of Physics and Astronomy, University of Minnesota, Minneapolis, Minnesota 55455, USA*

²*Stanford Institute for Materials and Energy Sciences, SLAC National Accelerator Laboratory, Menlo Park, CA 94025, USA*

³*Research Center for Electronic and Optical Materials, National Institute for Materials Science, 1-1 Namiki, Tsukuba 305-0044, Japan*

⁴*Research Center for Materials Nanoarchitectonics, National Institute for Materials Science, 1-1 Namiki, Tsukuba 305-0044, Japan*

⁵*School of Mathematics, University of Minnesota, Minneapolis, Minnesota 55455, USA*

⁶*Department of Physics, Harvard University, Cambridge, Massachusetts 02138, USA*

⁷*John A. Paulson School of Engineering and Applied Sciences, Harvard University, Cambridge, Massachusetts 02138*

**Corresponding author. Email: kewang@umn.edu*

We report a twisted triple bilayer graphene platform consisting of three units of Bernal bilayer graphene (BLG) consecutively twisted at 1.49° and 1.68° . We observe inter-moiré Hofstadter butterflies from two co-existing moiré superlattices and a Hofstadter butterfly from reconstructed moiré-of-moiré lattice, and show that their Brown-Zak (BZ) oscillations quantitatively agree with each other, both evidencing strong atomic reconstruction with a lattice constant of 18.1 nm. We further demonstrate such atomic reconstruction strongly enhances the Berry curvature of each moiré and moiré-of-moiré band-insulator state, characterized by measured strong non-local valley Hall effect (VHE) that sensitively depends on the inter-moiré competition strength, tunable by manipulating the out-of-the-plane carrier distribution which controls the magnitude of the valley currents. Our study sheds new light on the microscopic mechanism of atomic and electronic reconstruction in twisted-multilayer systems, by investigating novel emergent quantum phenomena of reconstructed quasi-crystalline moiré-of-moiré superlattice, including a new type of moiré-of-moiré band-insulator states and atomically enhanced moiré Berry curvature. We show that the reconstructed electronic band can be versatily tuned by electrostatics, providing an approach towards engineering the band structure and its topology for a novel quantum material platform with designer electrical and optical properties.

MAIN

The interference between two slightly rotated atomic lattices, which occurs at the homo- and hetero-interface of atomically thin materials stacked with small twist angles, gives rise to a moiré superlattice and flat bands where electronic interactions are enhanced. Novel material properties have been reported in such structures, including ferromagnetism¹, the quantum anomalous Hall effect²⁻⁴, quantum spin Hall effect⁵, Mott insulators⁶⁻⁸ and superconductivity^{9,10}.

Beyond twisted bilayers, the addition of a third 2D layer further enriches the emergent physics¹¹. When the third layer aligns with the first, the original moiré superlattice is atomically stabilized with enhanced correlated insulator and superconducting states¹²⁻¹⁴. When the third layer is mis-aligned with the existing layers, two separate moiré superlattices co-exist¹⁵⁻¹⁸. The beating between the two moiré superlattices gives rise to higher-order superlattices^{19,20}, referred to as moiré-of-moiré (MoM) superlattices. A wide range of competing length scales coexist, giving rise to an abundance of new electronic properties^{21,22}, including an inter-moiré Hofstadter butterfly¹⁷, quasi-crystal states¹⁶, correlated charge density wave

insulators²² and signatures of correlated insulating and superconducting states at an extremely low carrier density ($\sim 10^{10} \text{ cm}^{-2}$)²³.

To understand how competing atomic structures alter the resulting electronic band in a moiré-of-moiré superlattice, we fabricated twisted triple bilayer graphene (tTB LG) devices consisting of three units of Bernal bilayer graphene (BLG) consecutively twisted at 1.49° and 1.68° (see Fig. 1a and Methods). The choice of different twist angles ensures that the sizes of two co-existing moiré superlattices are sufficiently different (Fig. 1b, c), so that the transport signatures from each moiré lattice can be isolated and traced back to insulator states at different carrier densities, and the interaction between the moiré superlattices can be examined via emergent higher-order transport features at the carrier density in-between full fillings of the two individual moiré patterns. The choice of BLG as the basic unit of stacking allows for characterization of atomically induced band reconstruction by tracking the Berry curvature. Berry curvature hot spots were previously reported at the band edges of a parabolic-like band (at the charge neutrality point of a BLG or band insulator states of a moiré lattice)²⁴⁻²⁷, and can be sensitively enhanced by atomic strain/reconstruction from aligned hBN that further breaks the inversion symmetry²⁸.

Figure 1d shows the calculated band structure of tTB LG at the twist angles of 1.49° and 1.68° . The low-energy bands are parabolic instead of linear as in twisted bilayer or trilayer graphene, with the potential of hosting a Berry curvature hot spot at the band edges of moiré and MoM bands. Figure 1e shows the measured four-probe longitudinal resistance, R_{xx} , as a function of the displacement field, D (having the positive direction towards the graphite gate), and carrier density, n . The top (bottom) axis is given in terms of filling factors for top (bottom) moiré superlattices $\nu_T = 4n/n_T$ ($\nu_B = 4n/n_B$), where n_T (n_B) correspond to 4 charge carriers per top (bottom) moiré unit cell. Signature fillings from the top (bottom) moiré patterns are highlighted by yellow (purple) lines, where local resistance peaks are expected at integer fillings, including band-insulator states at full fillings (solid lines), and correlated insulator states at half fillings (dashed lines)²².

At $\nu_T = -4(+4)$, the hole-type (electron-type) charge carriers are localized in the top moiré superlattice by a positive (negative) D . The tTB LG in its entirety therefore exhibits insulating behavior, confirmed by the temperature dependence (Fig. 1f, g), with an estimated thermal activation gap of 5.6 ± 0.1 meV for $\nu_T = 4$ and 2.81 ± 0.03 meV for $\nu_T = -4$, respectively (see also Supplementary Information: S3). At $D = 0$, the transport signatures from both moiré superlattices are equally present and compete to determine the tTB LG electronic properties. The measured four-probe longitudinal resistance as a function of carrier density and magnetic field (Fig. 2a) shows complex Hofstadter butterfly²⁹⁻³² patterns, signatures of strongly interacting moiré superlattices and the resulting higher order MoM length scale.

In between $\nu_T = +4(-4)$ and $\nu_B = +4(-4)$, electron- (hole-) type Landau fans originating from the band insulator states of the two moiré lattices overlap to form an inter-moiré Hofstadter butterfly¹⁷ (Fig. 2b, c). In addition to the Shubnikov - de Haas (SdH) oscillations belonging to each fan, resistance dips are observed at $B = 7.2$ T, 4.8 T, 3.6 T, 2.8 T, 2.3 T, 2.0 T, ... manifesting as horizontal lines (dashed) or Brown-Zak oscillations in the inter-moiré butterfly^{17,33}, corresponding to $1/N$ (where $N = 2, 3, 4, 5, 6, 7 \dots$) flux quanta (ϕ_0) for a unit cell size of $284 \pm 6 \text{ nm}^2$ (or lattice constant of $18.1 \pm 0.2 \text{ nm}$) of the higher order MoM superlattice.

Remarkably, away from inter-moiré butterfly at $n = -1.4 \cdot 10^{12} \text{ cm}^{-2}$ (or 4 holes per unit cell of size 284 nm^2), a band insulator state (Fig. 1e) is observed at $D/\epsilon_0 < -0.4 \text{ V/nm}$ (Similarly for $D/\epsilon_0 > 0.4 \text{ V/nm}$, see Supplementary Information: S1). Its Hofstadter butterfly (conventional, overlapping with the fan from the charge neutrality point) demonstrates Brown-Zak oscillations (Fig. 2d) at $B = 7.2$ T, 4.8 T, 3.6 T, 2.8 T, 2.3 T, 2.0 T, same as the inter-moiré butterfly (Fig. 2b, c), confirming its origin as band-insulator states of the quasi-crystalline MoM superlattice, reconstructed from competing moiré superlattices. The common length scale of $18.1 \pm 0.2 \text{ nm}$ of inter-moiré (Fig. 2b, c) and MoM butterfly (Fig. 2d) correspond

to one of the dominating length scales of the simulated atomic landscape of tTBLG MoM superlattice (Fig. 2e), confirming that each moiré superlattice is experiencing a strong atomic and electronic modulation from the other.

In tTBLG, we show such modulation further enhances the Berry curvature of the moiré band insulator states, and can be sensitively manipulated by tuning the inter-moiré interaction strength. The Berry curvature is characterized with the well-established “non-local” measurement at $B = 0$ T^{25–28,34–38}. The valley-specific anomalous velocity drives the ballistic carrier trajectory astray (more so than conventional current diffusion^{25–28,34,36–39}), resulting in its detection at voltage probes sufficiently away from the current path.

We apply current I_{73} between contact 7 and 3 of the tTBLG device (Fig. 1b, 3a), and measure voltage V_{64} between contact 6 and 4 (as a result of transverse valley-polarized current) away from the current excitation (non-local) to study valley Hall effect (VHE)^{25–28,34,36–38,40,41}. The non-local resistance $R_{NL} = V_{64}/I_{73}$ as a function of the carrier density and D field is plotted in Fig. 3b. Non-local resistance peaks are found near $v_T = \pm 4$ and $D < 0$ ($D > 0$), satisfying pre-requisites for a Berry curvature hot spot: (1) Fermi level is near the edge of the band insulator gap, (2) the bottom BLG is depleted of charge carriers (so tTBLG is insulating with its Berry curvature well-defined). Similarly, non-local resistance peaks are found near $v_B = +4$ and $D > 0$, near the band-insulator gap of the bottom moiré while the top BLG is depleted of electron-type carriers. The absence of an expected non-local resistance peak near $v_B = -4$ at $D < 0$ is due to broken electron-hole symmetry in tTBLG, making such states less insulating or out of the measurement range.

These resistance peaks arise from the ballistic valley current driven by the Berry curvature, instead of stray currents due to diffusive Ohmic transport, supported by four separate experimental observations. First, the longitudinal resistance peaks (Fig. 1e) corresponding to the correlated insulator states are completely absent in the non-local measurement (Fig. 3b), confirming the origin of non-local resistance peaks as curved ballistic transport due to the Berry curvature, instead of a simple diffusive transport at resistive insulating states. Moreover, following previously-established methods^{25,27,28,34,38}, we measure the non-local signal R_{NL} at voltage probes with varying distance L to the applied current (see Supplementary Information: S5). The R_{NL} as a function of L is fitted by $\exp(-L/\xi)$, giving a decay length $\xi = 4 \pm 2$ μm , a change much slower than the decay due to diffusive Ohmic transport, and consistent with the inter-valley scattering length.

In addition, the trivial Ohmic contribution (R_{NLO}) from the stray currents can be estimated from the measured local (R_L) resistance by $R_{NLO} = R_L(w/L)\exp(-L/\lambda)$, where w , L are the length and width of the channel. Following previously well-established methods^{25–28,34}, the estimated Ohmic contribution can then be compared to the measured non-local resistance to understand the origin of measured R_{NL} . As an example (Fig. 3c), at $v_T = -4$ and $D/\epsilon_0 = +0.45$ V/nm, the measured non-local resistance R_{NL} is over 100 times larger than expected contribution from the diffusive Ohmic transport R_{NLO} (see Supplementary Information: S2 for other band-insulator states). The Ohmic contribution is therefore marginal, and the non-local resistance is primarily attributed to the Berry curvature.

Last but not least, the power-law scaling between the measured local and non-local resistances $R_{NL} \sim R_L^\gamma$ have been previously used to determine the nature of the non-local signal^{25–27,34,38,40}. Ohmic behavior is linear in nature ($\gamma = 1$), while non-local signal caused by the Berry curvature is expected to be non-linear, with either $\gamma > 1$ or $\gamma < 1$ depending on the saturation of ballistic valley current channel⁴⁰. In contrast to the previously reported Berry curvature hot spot in BLG, tBLG and tDBLG^{25–27,34}, the moiré Berry curvature hot spot in tTBLG shows an abrupt change across the band-insulator gap. To show this, the measured non-local resistance near $v_T = -4$ (Fig. 3c) is categorized into electron-type (blue) and hole-type (red). The R_{NL} versus R_L (Fig. 3d) is then separately plotted for each category of carrier type, and

individually fitted against $R_{NL} \sim R_L^\gamma$. Both show a good fit to a non-linear power law dependence, suggesting a Berry curvature hot spot as the underlying mechanism. The quantitative difference in the extracted power γ suggests that the Berry curvature hot spot shows a strong electron-hole asymmetry near $\nu_T = -4$, with the Berry curvature hot spot being stronger near the electron-type band edges of the $\nu_T = -4$, leading to a stronger valley Hall current (Fig. 3e, solid arrows) saturating the maximum current capacity of ballistic conductance channels with $\gamma < 1$ the reverse effect, weaker Berry curvature hot spot and valley Hall current, correspond to hole-type band edges, with $\gamma > 1$, see Fig. 3e, hollow black arrow)⁴⁰.

We show that the observed strong Berry curvature hot spot at $\nu_T = -4$ of the top moiré pattern is enhanced by the atomic reconstruction and electronic modification with the bottom moiré pattern, which further breaks the inversion symmetry and alters the band curvature. This can be demonstrated by measuring the power law γ (Fig. 3f), while tuning the strength of inter-moiré interaction with D ¹⁷. As the D field increases, the electron-type carrier is less localized in the top moiré pattern while its interaction with bottom moiré is enhanced leading to $\nu_T = -4$ band-insulator gaps whose Berry curvature is strongly reinforced by the presence of the bottom moiré pattern (the reverse effect corresponds to decreasing D field, with more localized carriers in the top moiré pattern and suppressed interaction with the bottom moiré pattern). As a result, the power law γ is observed to be continuously tunable by the field value (D) over one order of magnitude. At small D , when the inter-moiré interaction is weakest, the power law $\gamma = 3$ is similar to the previously reported valley Hall effect without an atomic reconstruction from aligned hBN^{28,38}. At large D , when the inter-moiré enhancement is strongest, the record-low $\gamma = 0.5$ suggests an unusually large valley Hall current driven by an extraordinarily-strong Berry curvature, over-saturating the available ballistic channels, more so than atomically-enhanced valley Hall effect previously reported in hBN-aligned systems^{28,38}.

In contrast, $\gamma = 3$ is observed for the hole-type carriers near $\nu_T = -4$, largely regardless of the D field applied. This suggests that the inter-moiré atomic reconstruction has much weaker implication to the hole-like band-edges, possibly due to a large electron-hole asymmetry in band dispersion or different ground state atomic orbitals for electrons and holes.

The non-local resistance R_{NL} peak at $\nu_T = -4$ is measured at varying temperature (Fig. 4a), from 10 mK to 20 K with an equal step size of $\Delta T \sim 2$ K. The resistance peak shows a weak temperature dependence below 10 K (with the curves for $T < 10$ K largely overlapping with each other), while drastically diminishes as T rises beyond 10 K. The change in temperature dependence can be seen more evidently when plotting R_{NL} as a function of temperature (Fig. 4b), measured at the peak (black) and half-height on the hole-like (red) and electron-like (blue), each showing a strong (weak) T -dependence beyond (below) $T \sim 10$ K.

All three data sets are fitted by $\exp\left(\frac{\Delta_{NL}}{2k_B T}\right)$ (Fig. 4b, dashed) for the temperature range above 10 K, each yielding a similar thermal activation gap Δ_{NL} . This is consistent with the non-local signal (peak or half-height) being expected only when the Fermi level is near mid-gap or at the band edges of the band insulator states. The displacement field dependence of the extracted Δ_{NL} (Fig. 4c) is also consistent with that of γ (Fig. 3f), with a larger Δ_{NL} being observed at higher D fields when stronger inter-moiré interaction further enhances the Berry curvature hot spot. At all values of the D field, Δ_{NL} is consistently larger than the thermal activation gaps Δ_L (Fig 4c, diamonds) extracted from the T -dependence of the longitudinal resistance $R_{xx}(T)$ at $\nu_T = -4$ (see Supplementary Information: S3).

The two energy scales near the band-insulator states are illustrated in Fig. 4d, each determining different aspects of the transport behavior near the Berry curvature hot spot: (1) the band insulator gap $\Delta_L = E_e - E_h$, defined as the difference between electron-like band minima E_e and hole-like band maxima E_h , the conventional definition of a bandgap; this gap determines the conventional transport such as R_{xx} . (2) The

non-local gap $\Delta_{NL} = E_e^* - E_h^*$, defined as the difference between the E_e^* and E_h^* , the energy in electron-like and hole-like bands, beyond which ($E > E_e^*$ and $E < E_h^*$) the Berry curvature becomes zero. This gap affects the anomalous transport aided by Berry curvature, such as R_{NL} .

The observed temperature dependence is consistent in each case with the Berry-curvature hot spot at $\nu_T = -4$, with a $\Delta_L = 3$ meV and $\Delta_{NL} = 10$ -15 meV. At temperature below 10 K (or $\Delta_{NL}/10$), additional carriers may be thermally excited across Δ_L , but they reside at band edges well within the Berry curvature hot spot (between E_e^* and E_h^*), equally capable of carrying valley Hall current that saturates the ballistic conductance channel. At temperature above 10 K (or $\sim \Delta_{NL}/10$), a significant portion of the carriers in the applied current start to fall energetically outside the Berry curvature hot spot, and thus stop experiencing the anomalous velocity, no longer contributing to the non-local signal, hence the change of temperature dependence (Fig. 4a, b) of R_{NL} at $T \sim 10$ K, and a significantly larger Δ_{NL} (Fig. 4c) that more sensitively depends on the D field applied compared to Δ_L . This implies that the enhancement of the Berry curvature hot spot (characterized by Δ_{NL}) is more attributed to the inter-moiré interaction than the evolution of the band structure itself (characterized by Δ_L).

We have also observed transport signatures of a Berry curvature hot spot at a carrier density $n = -1.4 \cdot 10^{12}$ cm⁻² (Fig. 5a), corresponding to 4 carriers per MoM unit cell given by the BZ oscillations in the inter-moiré and MoM butterfly. This confirms the nature of these states as MoM band insulator states instead of moiré correlated insulator states. Similar to the moiré Berry curvature hot spot, the non-local resistances near the MoM Berry curvature hot spot exhibit an electron-hole asymmetric non-ohmic behavior (Fig. 5b). In contrast to the moiré Berry curvature hot spot that can be enhanced by inter-moiré reconstruction all the way to $\gamma = 0.5$, the moiré-of-moiré Berry curvature has a power law scaling γ consistently larger than 1, which displays a weaker D field dependence (Fig. 5c). This suggests the MoM Berry curvature hot spot is only capable of promoting a moderate valley Hall current far from saturation, similar to the previously reported system without an additional atomic reconstruction from aligned hBN²⁸. This difference is consistent with the picture of the inter-moiré atomic reconstruction being primarily responsible for the Berry curvature enhancement. As the MoM band-insulator state is constructed by all three components of BLG acting together, its Berry curvature does not benefit from the atomic reconstruction the way moiré Berry curvature does, due to the absence of an additional atomic layer. This is further supported by the temperature dependence of MoM valley Hall effect (Fig. 5d-f). While the extracted Δ_{NL} is still consistently larger than Δ_L (confirming the existence and extent of the Berry curvature hot spot), its value shows little D field dependence, and is comparable only to that of moiré band-insulator states at lower D field when inter-moiré interaction is suppressed, and moiré Berry curvature is not effectively enhanced.

In conclusion, we studied twisted triple bilayer graphene devices with consecutive twist angles of 1.49° and 1.68°, in which atomic and electronic reconstruction between two co-existing moiré superlattices gives rise to a higher-order moiré-of-moiré superlattices and an enhanced moiré Berry curvature hot spot. The BZ oscillations from the two sets inter-moiré Hofstadter butterflies and the moiré-of-moiré Hofstadter butterflies all correspond to the same higher-order moiré-of-moiré length scale, confirming the existence of the inter-moiré atomic reconstruction. Such atomic reconstruction enhances the Berry curvature of the moiré band-insulator states, characterized by measured strong non-local valley Hall effect, which depends sensitively on electrostatically tuned inter-moiré competition strength, supporting several orthogonal sets of experimental observations. Our study sheds new light on the microscopic nature of atomic and electronic properties of the moiré-of-moiré superlattice, providing an approach towards engineering the band structure and its topology for a novel quantum material platform with designer electrical and optical properties.

METHODS

The dual-gated twisted triple bilayer graphene (tTBLG) stack was made using the “cut and tear” method¹⁰. A single bilayer graphene (BLG) flake was cut into three individual pieces with the same lattice orientation using the cantilever of an XE7 atomic force microscope (AFM) from Park Systems. Using a poly (bisphenol A carbonate) (PC) and polydimethylsiloxane (PDMS) stamp mounted on a glass slide, a top hexagonal boron nitride⁴² (hBN) flake, few-layer graphite (serving as the top gate) and middle hBN (isolating the graphite gate from tTBLG) were picked up. Next, the three pre-cut pieces of BLG were successively picked up. After each pick up step, the remaining pieces of BLG were rotated at angles of 1.49° and 1.68° in the same direction. Finally, the tTBLG was encapsulated by picking up a bottom hBN, and the complete stack was released onto a SiO₂(285 nm)/Si substrate at 180 °C. The PC residue on top of the stack was cleaned by sequentially rinsing the chip containing the stack in chloroform, acetone and isopropanol. Afterwards, a bubble free area of the device serving as the active region was found using the AFM, ensuring the high quality of the device. Ohmic contacts⁴³ to 1D boundaries of the tTBLG were then added using electron-beam lithography, dry-etching, and subsequent metal deposition (Cr/Pd/Au, 1 nm / 5 nm / >180 nm). Finally, the active region was given a Hall bar shape (Fig. 1b) by a round of electron-beam lithography and reactive ion dry-etching.

The electrical- and magneto-transport measurements were performed in a Bluefors LD250 cryostat at base temperature of $T = 10$ mK and temperatures ranging from 10mK to 20K (for T-dependence) with magnetic fields up to 8T. The four-probe measurements of the device were performed with 0.5, 1, 10, and 200 nA AC current excitations at a frequency of 17.777 Hz. The voltage drops across the device were measured with the help of SR830 lock-in amplifiers (Stanford Research Systems). The top and back gate voltages were controlled by two voltage sources (Yokogawa: Model GS200 and Keithley Instruments: Model 2400 respectively).

ACKNOWLEDGEMENTS

We thank Andrey Chubukov and Boris Shklovskii for useful discussions. This work was supported by NSF DMREF Award 1922165 and ARO MURI Grant No. W911NF-14-1-0247. Z.Z. is supported by a Stanford Science Fellowship. EK acknowledges support from Simons Foundation Award no. 896626. Nanofabrication was conducted in the Minnesota Nano Center, which is supported by the National Science Foundation through the National Nanotechnology Coordinated Infrastructure (NNCI) under Award Number ECCS-2025124. Portions of the hexagonal boron nitride material used in this work were provided by K.W and T. T. K.W. and T.T. acknowledge support from the JSPS KAKENHI (Grant Numbers 20H00354, 21H05233 and 23H02052) and World Premier International Research Center Initiative (WPI), MEXT, Japan

REFERENCES

1. Sharpe, A. L. *et al.* Emergent ferromagnetism near three-quarters filling in twisted bilayer graphene. *Science* **365**, 605–608 (2019).
2. Park, H. *et al.* Observation of fractionally quantized anomalous Hall effect. *Nature* **622**, 74–79 (2023).

3. Reddy, A. P., Alsallom, F., Zhang, Y., Devakul, T. & Fu, L. Fractional quantum anomalous Hall states in twisted bilayer MoTe₂ and WSe₂. *Phys. Rev. B* **108**, 085117 (2023).
4. Xu, F. *et al.* Observation of Integer and Fractional Quantum Anomalous Hall Effects in Twisted Bilayer MoTe₂. *Phys. Rev. X* **13**, 031037 (2023).
5. Kang, K. *et al.* Evidence of the fractional quantum spin Hall effect in moiré MoTe₂. *Nature* 1–5 (2024) doi:10.1038/s41586-024-07214-5.
6. Cao, Y. *et al.* Correlated insulator behaviour at half-filling in magic-angle graphene superlattices. *Nature* **556**, 80–84 (2018).
7. Nuckolls, K. P. *et al.* Strongly correlated Chern insulators in magic-angle twisted bilayer graphene. *Nature* **588**, 610–615 (2020).
8. Wu, S., Zhang, Z., Watanabe, K., Taniguchi, T. & Andrei, E. Y. Chern insulators, van Hove singularities and topological flat bands in magic-angle twisted bilayer graphene. *Nat. Mater.* **20**, 488–494 (2021).
9. Cao, Y. *et al.* Unconventional superconductivity in magic-angle graphene superlattices. *Nature* **556**, 43–50 (2018).
10. Saito, Y., Ge, J., Watanabe, K., Taniguchi, T. & Young, A. F. Independent superconductors and correlated insulators in twisted bilayer graphene. *Nat. Phys.* **16**, 926–930 (2020).
11. Zhu, Z., Carr, S., Massatt, D., Luskin, M. & Kaxiras, E. Twisted Trilayer Graphene: A Precisely Tunable Platform for Correlated Electrons. *Phys. Rev. Lett.* **125**, 116404 (2020).
12. Hao, Z. *et al.* Electric field-tunable superconductivity in alternating-twist magic-angle trilayer graphene. *Science* **371**, 1133–1138 (2021).
13. Park, J. M., Cao, Y., Watanabe, K., Taniguchi, T. & Jarillo-Herrero, P. Tunable strongly coupled superconductivity in magic-angle twisted trilayer graphene. *Nature* **590**, 249–255 (2021).

14. Shin, J., Chittari, B. L., Jang, Y., Min, H. & Jung, J. Nearly flat bands in twisted triple bilayer graphene. *Phys. Rev. B* **105**, 245124 (2022).
15. Wang, L. *et al.* New Generation of Moiré Superlattices in Doubly Aligned hBN/Graphene/hBN Heterostructures. *Nano Lett.* **19**, 2371–2376 (2019).
16. Uri, A. *et al.* Superconductivity and strong interactions in a tunable moiré quasiperiodic crystal. Preprint at <http://arxiv.org/abs/2302.00686> (2023).
17. Ren, W. *et al.* Tunable Inter-Moiré Physics in Consecutively-Twisted Trilayer Graphene. Preprint at <https://doi.org/10.48550/arXiv.2311.10313> (2023).
18. Yang, C., May-Mann, J., Zhu, Z. & Devakul, T. Multi-moiré trilayer graphene: lattice relaxation, electronic structure, and magic angles. Preprint at <https://doi.org/10.48550/arXiv.2310.12961> (2023).
19. Zhu, Z., Cazeaux, P., Luskin, M. & Kaxiras, E. Modeling mechanical relaxation in incommensurate trilayer van der Waals heterostructures. *Phys. Rev. B* **101**, 224107 (2020).
20. Park, D. *et al.* Tunable incommensurability and spontaneous symmetry breaking in the reconstructed moiré-of-moiré lattices. Preprint at <https://doi.org/10.48550/arXiv.2402.15760> (2024).
21. Devakul, T. *et al.* Magic-angle helical trilayer graphene. *Science Advances* **9**, eadi6063 (2023).
22. Wang, W. *et al.* Correlated Charge Density Wave Insulators in Chirally Twisted Triple Bilayer Graphene. *Phys. Rev. Lett.* **132**, 246501 (2024).
23. Zhang, X. *et al.* Correlated Insulating States and Transport Signature of Superconductivity in Twisted Trilayer Graphene Superlattices. *Phys. Rev. Lett.* **127**, 166802 (2021).
24. Novoselov, K. S. *et al.* Unconventional quantum Hall effect and Berry's phase of 2π in bilayer graphene. *Nature Phys* **2**, 177–180 (2006).
25. Shimazaki, Y. *et al.* Generation and detection of pure valley current by electrically induced Berry curvature in bilayer graphene. *Nature Phys* **11**, 1032–1036 (2015).

26. Sui, M. *et al.* Gate-tunable topological valley transport in bilayer graphene. *Nature Phys* **11**, 1027–1031 (2015).
27. Sinha, S. *et al.* Bulk valley transport and Berry curvature spreading at the edge of flat bands. *Nat Commun* **11**, 5548 (2020).
28. Gorbachev, R. V. *et al.* Detecting topological currents in graphene superlattices. *Science* **346**, 448–451 (2014).
29. Hofstadter, D. R. Energy levels and wave functions of Bloch electrons in rational and irrational magnetic fields. *Phys. Rev. B* **14**, 2239–2249 (1976).
30. Dean, C. R. *et al.* Hofstadter’s butterfly and the fractal quantum Hall effect in moiré superlattices. *Nature* **497**, 598–602 (2013).
31. Hunt, B. *et al.* Massive Dirac Fermions and Hofstadter Butterfly in a van der Waals Heterostructure. *Science* **340**, 1427–1430 (2013).
32. Ponomarenko, L. A. *et al.* Cloning of Dirac fermions in graphene superlattices. *Nature* **497**, 594–597 (2013).
33. Jat, M. K. *et al.* Higher order gaps in the renormalized band structure of doubly aligned hBN/bilayer graphene moiré superlattice. *Nat. Commun.* **15**, 2335 (2024).
34. Ma, C. *et al.* Moiré Band Topology in Twisted Bilayer Graphene. *Nano Lett.* **20**, 6076–6083 (2020).
35. Abanin, D. A. *et al.* Giant Nonlocality Near the Dirac Point in Graphene. *Science* **332**, 328–330 (2011).
36. Salvador-Sánchez, J. *et al.* Generation and control of nonlocal chiral currents in graphene superlattices by orbital Hall effect. *Phys. Rev. Res.* **6**, 023212 (2024).
37. Komatsu, K. *et al.* Observation of the quantum valley Hall state in ballistic graphene superlattices. *Science Advances* **4**, eaaq0194 (2018).

38. Li, Y., Amado, M., Hyart, T., Mazur, G. P. & Robinson, J. W. A. Topological valley currents via ballistic edge modes in graphene superlattices near the primary Dirac point. *Commun Phys* **3**, 1–7 (2020).
39. Xiao, D., Chang, M.-C. & Niu, Q. Berry phase effects on electronic properties. *Rev. Mod. Phys.* **82**, 1959–2007 (2010).
40. Beconcini, M., Taddei, F. & Polini, M. Nonlocal topological valley transport at large valley Hall angles. *Phys. Rev. B* **94**, 121408 (2016).
41. Liu, J., Ma, Z., Gao, J. & Dai, X. Quantum Valley Hall Effect, Orbital Magnetism, and Anomalous Hall Effect in Twisted Multilayer Graphene Systems. *Phys. Rev. X* **9**, 031021 (2019).
42. Dean, C. R. *et al.* Boron nitride substrates for high-quality graphene electronics. *Nat. Nanotechnol.* **5**, 722–726 (2010).
43. Wang, L. *et al.* One-dimensional electrical contact to a two-dimensional material. *Science* **342**, 614–617 (2013).

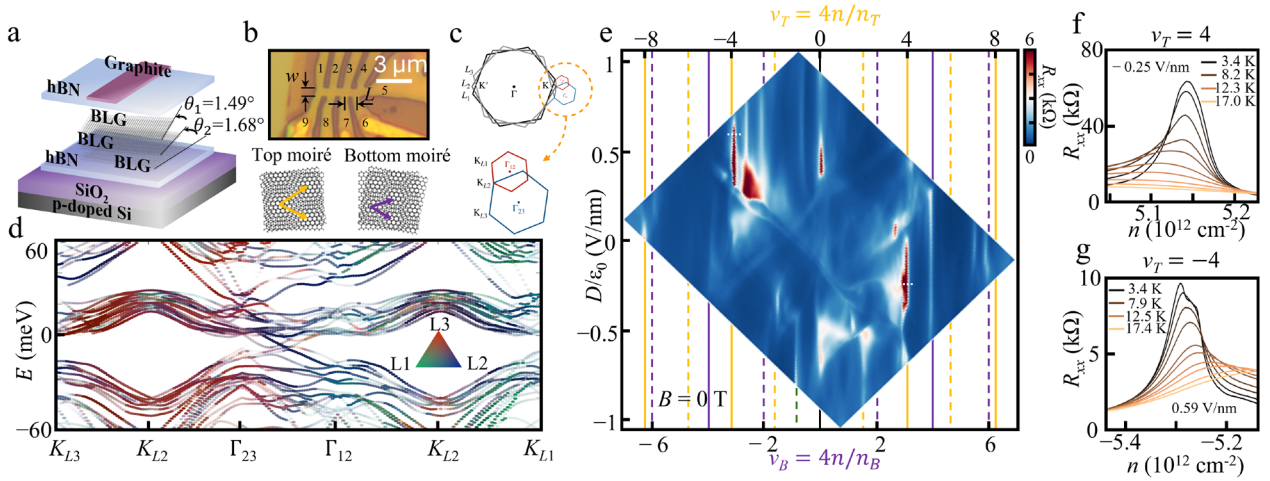


Figure 1 | Gate-tunable insulating states of competing moiré superlattices in tTB LG. **a**, Schematic architecture of the dual gated tTB LG stack with the two consecutive twist angles of 1.49° and 1.68° . **b**, Upper: optical micrograph of the Hall bar shaped tTB LG device with L and w being the length and width of the channel. Lower: schematic images of the coexisting top (bottom) moiré superlattices, with the yellow (purple) arrows indicating the corresponding unequal superlattice vectors. **c**, Top: the relative position of the Brillouin zones of each of the three BLGs. Bottom: the alignment of the two mini-Brillouin zones of different sizes corresponding to the top and bottom moirés. **d**, Calculated band structure of tTB LG at the twist angles of 1.49° and 1.68° along high symmetry points of the mini-Brillouin zones. Colors indicate the projected weight of each BLG layer. Top layer: green; middle layer: blue; bottom layer: red. **e**, The measured four-probe longitudinal resistance, R_{xx} , as a function of the top (bottom) moiré filling factors and displacement field, D . Displacement field asymmetric insulating states are observed at full (solid lines) and half (dashed lines) fillings of the two moirés. **f**, **g**, Temperature dependence of R_{xx} of the $\nu_T = 4$ (-4) states at $D/\epsilon_0 = -0.25$ V/nm (0.59 V/nm) within the temperature ranges between 3.4 K and 17 K (3.4 K and 17.4 K) taken at a step of $\Delta T \sim 1.5$ K. The steep decrease of R_{xx} at $T > 10$ K confirms the insulating behavior of the tTB LG.

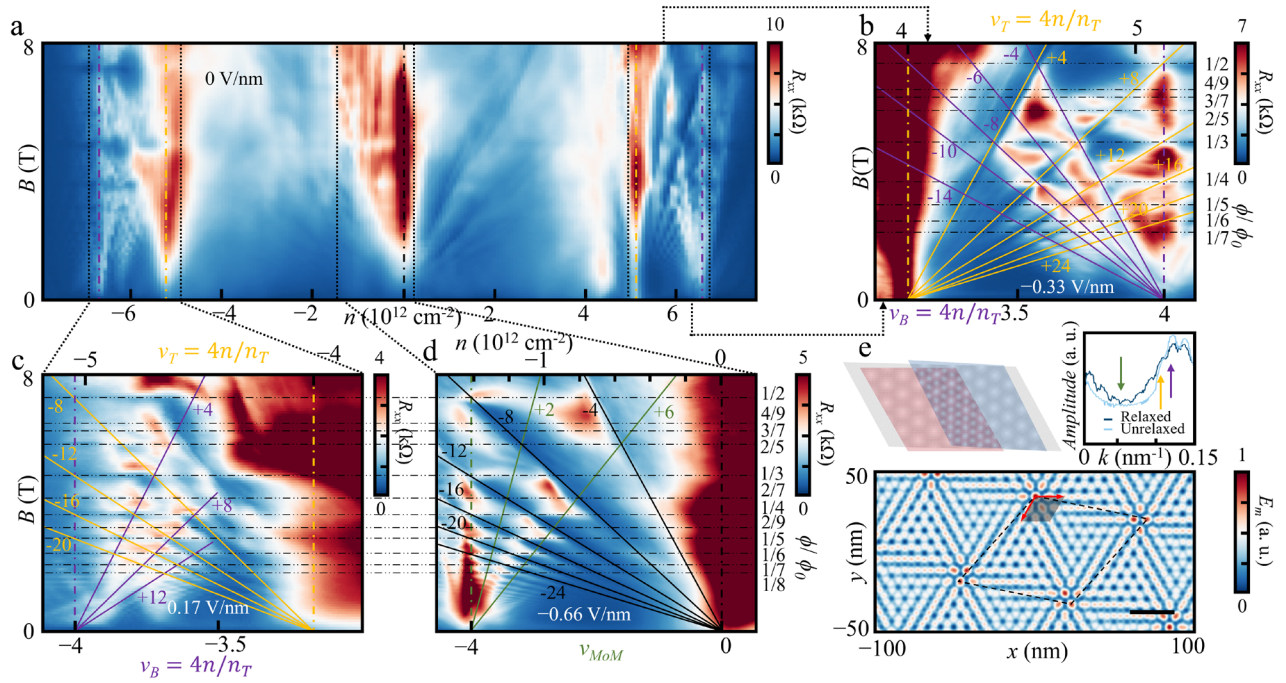


Figure 2 | Inter-moiré and moiré-of-moiré Hofstadter butterflies. **a**, R_{xx} as a function of magnetic field and charge carrier density at zero displacement field showing two sets of Landau fans corresponding to the top and bottom moirés. **b**, Inter-moiré Hofstadter butterfly emerging on the electron-doped side when the Landau fans from the top and bottom moirés overlap at $D/\epsilon_0 = -0.33$ V/nm. The solid lines trace SdH oscillations from the band insulator states of each moiré. The horizontal dashed lines trace the BZ oscillations at $\phi/\phi_0 = p/N$, with p, N being integers indicated on the right. **c**, Same as **b** but on the hole side and at $D/\epsilon_0 = 0.17$ V/nm. **d**, Moiré-of-moiré Hofstadter butterfly near the charge neutrality point with the BZ oscillations' periodicity matching that of the inter-moiré Hofstadter butterfly. The SdH periodicity of the MoM Landau fan is consistent with its band insulator behavior. **e**, Upper left: two coexisting moiré lattice periodicities resulting in a third (middle region) from the two top (red) and two bottom (blue) BLG layers. Lower: simulated relaxed energy landscape of the tTBLG with the color representing the total misfit energy. The unit cell (shaded in gray) with an area of 284 ± 6 nm 2 is extracted from the BZ oscillations corresponding to the lattice vectors (red arrows) with length 18.1 ± 0.2 nm. The scale bar is 30 nm. Upper right: Fourier spectrum of the relaxed and unrelaxed atomic landscape with the characteristic top (yellow 9.5 nm) and bottom (purple, 8.4 nm) moiré length scales indicated by the arrows. The green arrow marks the MoM periodicity (18.1 nm) in **d** extracted from the BZ oscillations.

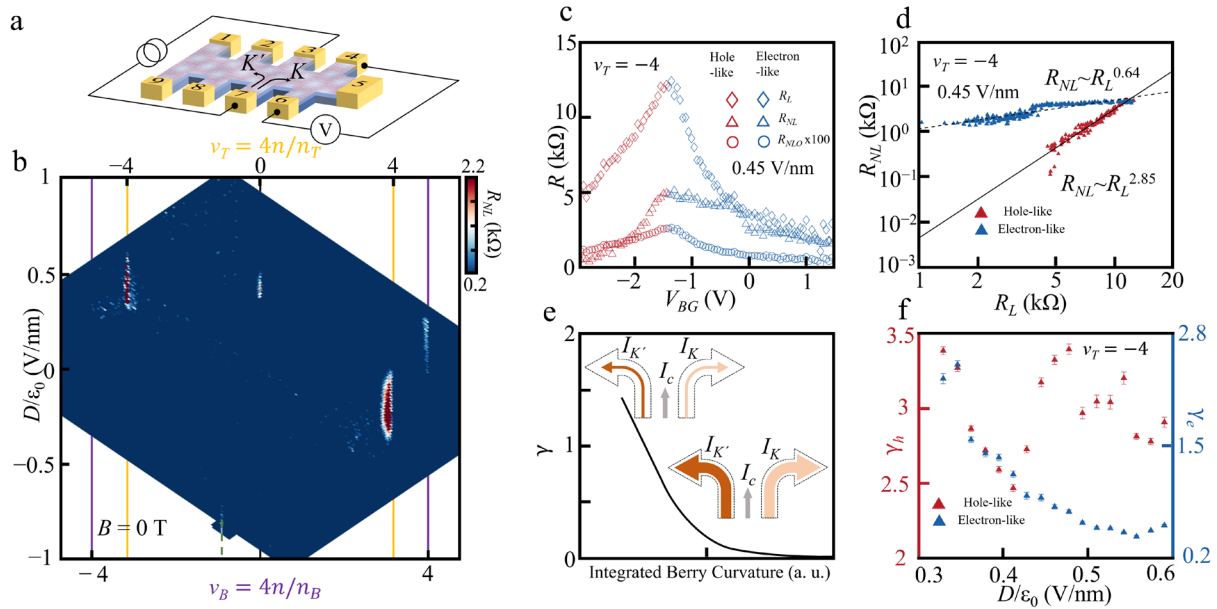


Figure 3 | Atomic lattice reconstruction enhanced Berry curvature hot spot. **a**, Non-local signal measurement configuration with currents from the different valleys bending in the opposite directions resulting in a transverse valley current. **b**, Measured non-local resistance, $R_{NL} = V_{64}/I_{73}$ (ratio between the measured non-local voltage and driven current), as a function of D and n . Five peaks are visible corresponding to different Berry curvature hot spots. **c**, Non-local (R_{NL}), local (R_L), and non-local Ohmic (R_{NLO}) resistances due to the stray charge currents near $\nu_T = -4$ and at $D/\epsilon_0 = +0.45$ V/nm. **d**, R_{NL} versus R_L for hole-like (red) and electron-like (blue) carriers near $\nu_T = -4$ at $D/\epsilon_0 = +0.45$ V/nm. The solid and dashed lines correspond to power law fits for the hole- and electron-like carriers. **e**, Qualitative evolution of the power law dependence $R_{NL} \sim R_L^\gamma$ as a function of magnitude of the integrated Berry curvature. The inset shows the change in the relative magnitudes of the charge (I_c) and the corresponding valley currents ($I_K, I_{K'}$) as the Berry curvature (and thus, the ratio between the valley Hall and charge conductance) increases. **f**, Displacement field dependence of the powers of the $R_{NL} \sim R_L^{\gamma^h}$ ($R_{NL} \sim R_L^{\gamma^e}$) laws for the hole- (electron-) like charge carriers.

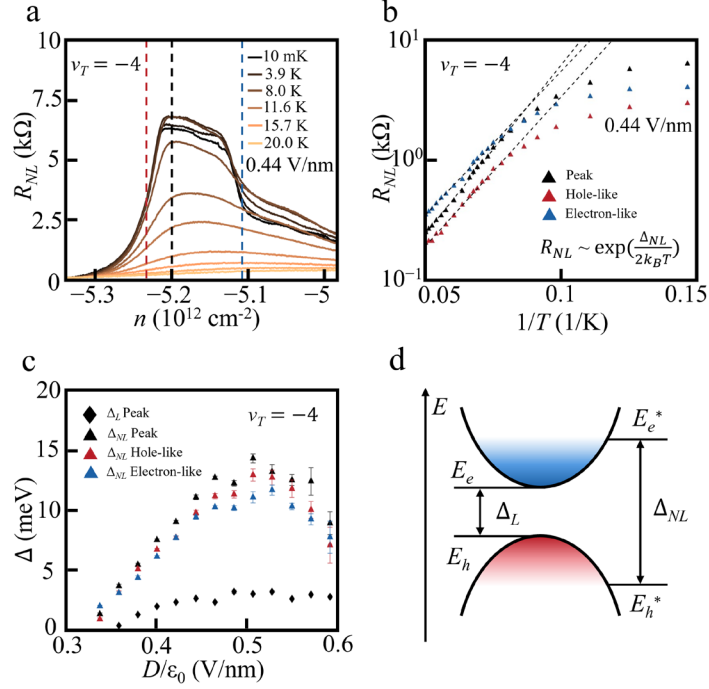


Figure 4 | Temperature dependence of valley Hall effect. **a**, Thermal activation behavior of R_{NL} near $v_T = -4$ at $D/\epsilon_0 = +0.44$ V/nm. The black dashed line indicates the position of the peak resistance at 10 mK; the blue and red dashed lines trace R_{NL} at half the peak height at 10 mK for the electron- and hole-like charge carriers respectively. The temperature increases from 10 mK to 20 K with an increment of $\Delta T \sim 2$ K. **b**, Temperature dependence of the peak (black) and half-peak R_{NL} for the electron-like (blue) and hole-like (red) carriers. The dashed lines represent Arrhenius fits at high temperatures. **c**, The size of the local (Δ_L) and non-local (Δ_{NL}) bandgaps found from the Arrhenius fits of the peak (black) and half-peak (blue and red, matching the carrier type) value of the resistance as a function of D . **d**, Illustration of different energy scales of a Berry curvature hot spot. The local band gap, Δ_L , matches the band insulator gap and equals the difference between the conduction and valence band edges energies, E_e and E_h . The size of the non-local band gap, $\Delta_{NL} = E_e^* - E_h^*$, determined by the energies E_e^* (E_h^*) above (below) which the Berry curvature labeled by blue (red) in the electron- (hole-) band vanishes.

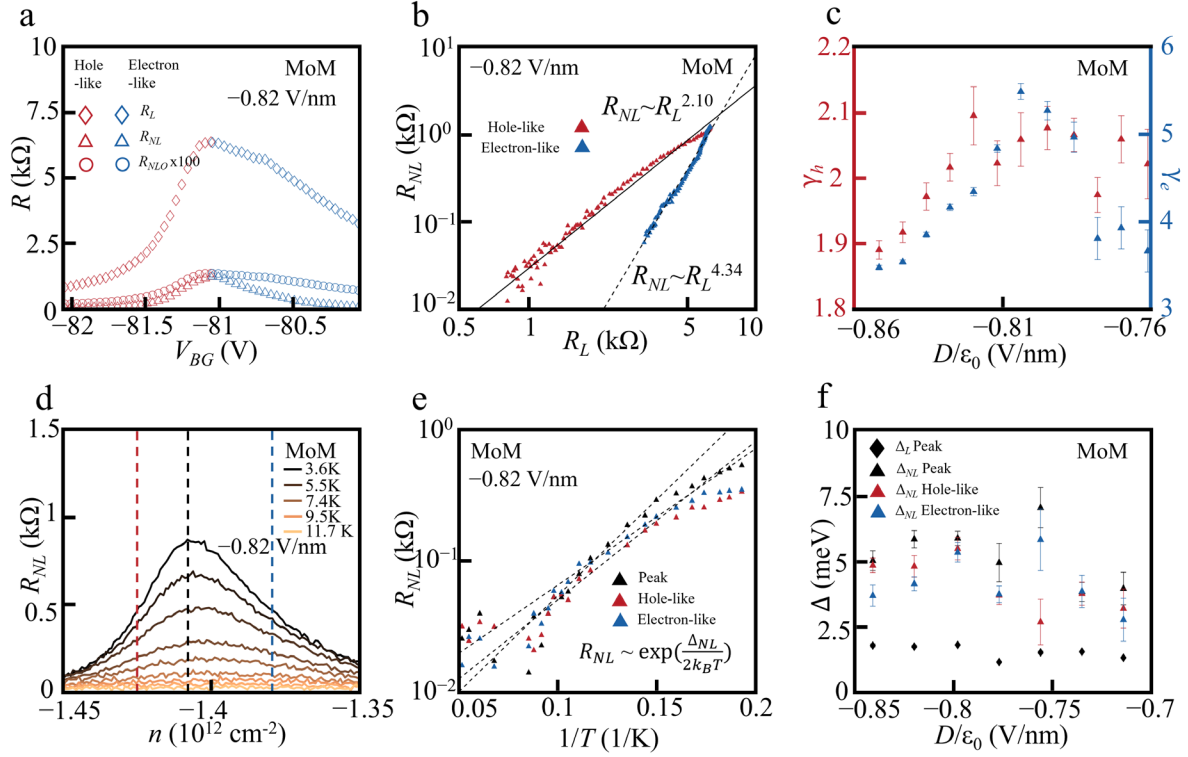


Figure 5 | Valley Hall effect and Berry curvature of moiré-of-moiré band insulator state. **a**, Non-local (R_{NL}), local (R_L), and non-local Ohmic (R_{NLO}) resistances near the moiré-of-moiré (MoM) band insulator (BI) at $D/\epsilon_0 = -0.82$ V/nm. **b**, The dependence of R_{NL} on R_L for hole-like (red) and electron-like (blue) carriers near the MoM BI at $D/\epsilon_0 = -0.82$ V/nm. The solid and dashed lines represent power law fits for the hole- and electron-like carriers across the MoM band insulator gap. **c**, Displacement field dependence of the exponents in the power law fits for the hole-like (exponent, γ_h) and electron-like (exponent, γ_e) charge carriers near the MoM BI. **d**, Decreasing with temperature R_{NL} near the MoM BI at $D/\epsilon_0 = -0.82$ V/nm between $T = 3.6$ K and 11.7 K with an increment of $\Delta T \sim 1$ K. The black dashed line indicates the maximum non-local resistance at 3.6 K; the blue and red lines trace R_{NL} at half the maximum of R_{NL} at 3.6 K for the electron and hole-like charge carriers respectively. **e**, Peak (black) and half-peak R_{NL} for the electron-like (blue) and hole-like (red) carriers as a function of inverse temperature. Arrhenius fits at high temperatures are shown as dashed lines. **f**, Displacement field dependence of the local (Δ_L) and non-local (Δ_{NL}) bandgaps extracted from the Arrhenius fits of the peak (black) and half-peak (blue and red, matching the carrier type) value of the resistance.

Tunable atomically enhanced moiré Berry curvatures in twisted triple bilayer graphene

Konstantin Davydov¹, Ziyang Zhu², Noah Friedman¹, Ethan Gramowski¹, Yaotian Li¹, Jack Tavakley¹, Kenji Watanabe³, Takashi Taniguchi⁴, Mitchell Luskin⁵, Efthimios Kaxiras^{6,7}, Ke Wang^{1*}

¹*School of Physics and Astronomy, University of Minnesota, Minneapolis, Minnesota 55455, USA*

²*Stanford Institute for Materials and Energy Sciences, SLAC National Accelerator Laboratory, Menlo Park, CA 94025, USA*

³*Research Center for Electronic and Optical Materials, National Institute for Materials Science, 1-1 Namiki, Tsukuba 305-0044, Japan*

⁴*Research Center for Materials Nanoarchitectonics, National Institute for Materials Science, 1-1 Namiki, Tsukuba 305-0044, Japan*

⁵*School of Mathematics, University of Minnesota, Minneapolis, Minnesota 55455, USA*

⁶*Department of Physics, Harvard University, Cambridge, Massachusetts 02138, USA*

⁷*John A. Paulson School of Engineering and Applied Sciences, Harvard University, Cambridge, Massachusetts 02138*

*Corresponding author. Email: kewang@umn.edu

S1. Displacement field dependence of inter-moiré and moiré-of-moiré Hofstadter butterflies

The competition between the two moiré length scales facilitates atomic lattice reconstruction yielding a complex moiré-of-moiré (MoM) structural landscape having a plethora of spatial periodicities (Fig. 1e). Applying an out-of-plane displacement field, D , leads to charge redistribution between the two moirés tuning their contribution to electrical transport measurements. In the range of D when charge carriers occupy both inter-layer interfaces, signatures of both moiré band-insulator states are present. In this regime, the interaction and competition between the two moirés is enhanced giving the most prominent effect on magnetoresistance. In particular, at $n_T < |n| < n_B$, R_{xx} shows B field dependent dips (Brown-Zak oscillations) with the periodicity determined by reconstruction between the two moirés and corresponding to one of the MoM spatial periodicities. For electron doped tTBLG at -0.33 V/nm $\leq D/\epsilon_0 \leq 0.17$ V/nm (Fig. S1, a-d) both moirés have comparable contribution, yielding well-defined band-insulator states at $\nu_T, \nu_B = 4$. As a result, a clear inter-moiré Hofstadter butterfly is observed with BZ oscillations consistent with the MoM lattice constant of 18.1 ± 0.2 nm. Further increasing the displacement field pushes the electrons from the top moiré interface thus diminishing its contribution (which can be seen as the absence of the SdH oscillations' dips in Fig. 1e) to defining the inter-moiré Hofstadter spectrum. Similar effects can be observed for the hole-type inter-moiré butterfly (Fig. S1, f-j). When the holes are present on the top and bottom moiré interfaces at -0.17 V/nm $\leq D/\epsilon_0 \leq 0.17$ V/nm (Fig. S1, g-i) and are equally contributing to the inter-moiré interaction, a clear Hofstadter butterfly can be observed. Decreasing (increasing) D (Fig. S1, f-j) leaves only the bottom (top) moiré to dominate, showing ill-defined signatures of a Hofstadter butterfly due to suppressed inter-moiré interaction.

The same MoM periodicity giving rise to the inter-moiré Hofstadter butterflies causes band folding, resulting in band-insulator (BI) states near the CNP. At four holes per MoM unit cell with a lattice constant of 18.1 nm corresponding to $n = -1.4 \cdot 10^{12}$ cm⁻², and with $D/\epsilon_0 < -0.4$ V/nm, a BI is observed manifesting as a resistance peak (Fig. 1e). Under applied B field, R_{xx} displays a Hofstadter butterfly (Fig. S2, a-c) with the same BZ oscillation periodicity as the inter-moiré case

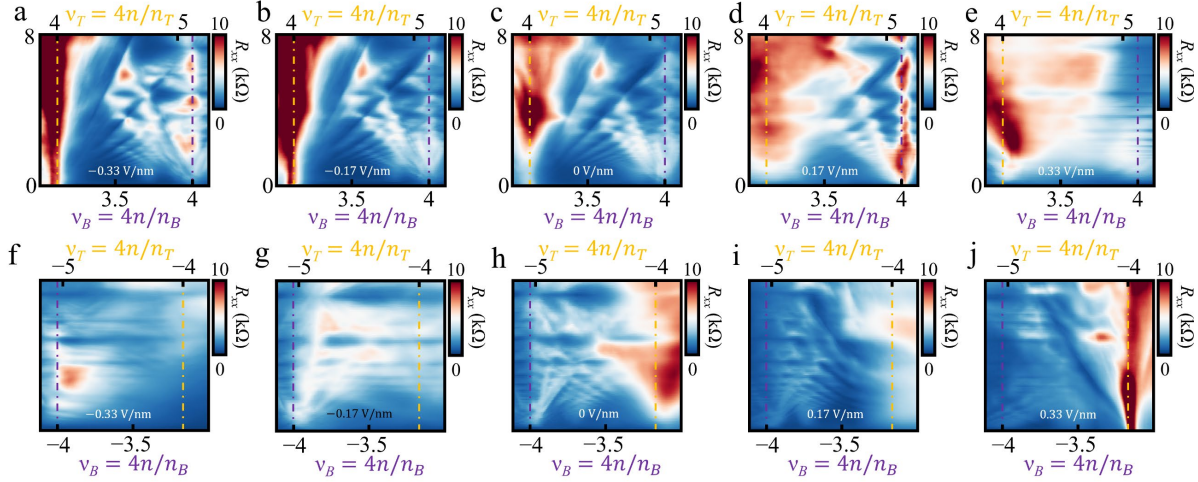


Figure S1 | Displacement field dependence of inter-moiré Hofstadter butterfly. a-e, Longitudinal resistance, R_{xx} , as a function of magnetic field and top (ν_T), bottom (ν_B) moiré filling factors at different displacement fields between -0.33V/nm and 0.33 V/nm . The charge carrier densities correspond to a range between four electrons per top and bottom moiré unit cell area. Increasing D depletes the top moiré interface from electrons suppressing the inter-moiré interaction resulting in suppressed Hofstadter butterfly spectrum. f-j, Same as a-e but charge carrier density is in the range between four holes per top and bottom moiré unit cell. In the range of $-0.17\text{ V/nm} \leq D/\epsilon_0 \leq 0.17\text{ V/nm}$, when none of the moirés dominate, the interaction and competition between the two moirés gives rise to an inter-moiré Hofstadter butterfly spectrum.

due to the same MoM lattice with a period of 18.1 nm. Decreasing the D field gives more prominent Hofstadter butterfly signatures. Conversely, a more positive D makes the Hofstadter spectrum less defined (Fig. S2, d-f). By further increasing D/ϵ_0 beyond 0.4 V/nm, another Hofstadter butterfly consistent with the length scale of 19.8 nm (Fig. S3, g-i) can be seen. The same periodicity results in a MoM BI state at $n = (-1.1 \pm 0.2) \cdot 10^{12}\text{ cm}^{-2}$ manifested as a resistance peak corresponding to four holes per MoM unit cell with the lattice vector of 19.8 nm.

S2. Valley Hall effect from additional band insulator states

The valley Hall effect can be observed at multiple BI states in the tTB LG device. In addition to the $\nu_T = -4$ and MoM BI states, Berry curvature hot spots are present near the $\nu_T = 4$ and $\nu_B = 4$ fillings (Fig. 3b). At both fillings, non-local measurements following the protocol from the main manuscript demonstrate a non-local resistance more than one order of magnitude larger than trivial Ohmic contribution due to stray currents (Fig S3a, b). Figures S3, c, and d, show the non-local resistance, R_{NL} , as a function of the local one, R_L , near the $\nu_T = 4$ and $\nu_B = 4$ fillings respectively. The plotted resistance dependence shows a clear difference for the hole-like (red) and electron-like (blue) carriers changing their type across the BI state. The non-local resistance for each carrier type follows a non-linear power law relationship, $R_{NL} \sim R_L^\gamma$, with the power, $\gamma = \gamma_h$ (γ_e), extracted from separate fittings for hole- (electron-) like R_{NL} . Both powers being sufficiently different from $\gamma = 1$ at varying D (Fig. S3e, f) indicate a non-Ohmic mechanism of non-local transport through valley current due to a Berry curvature hot spot. When the ballistic valley-chiral channel is completely saturated, the power γ reaches zero. In the opposite scenario, when the

valley-chiral channel is established, yet far from saturation, the power is expected to approach $\gamma \rightarrow 3$.

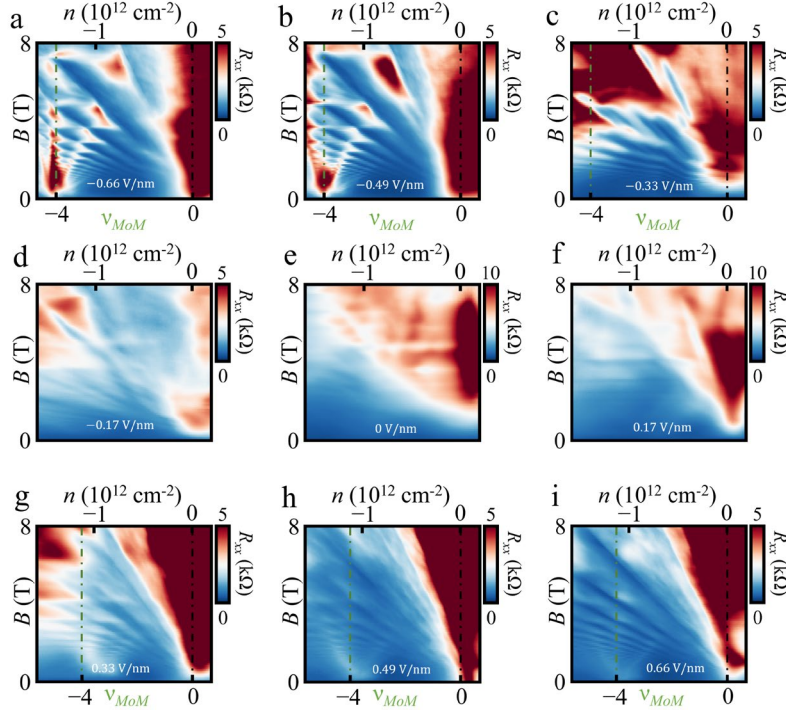


Figure S2 | Displacement field dependence of moiré-of-moiré Hofstadter butterfly. **a-c**, R_{xx} depending on magnetic field, B , and charge carrier density, n , at different displacement fields (from -0.66V/nm to -0.33 V/nm). A satellite Landau fan corresponding to MoM BI state emanating at four holes (green dashed line) per MoM unit cell (having a lattice constant of 18.1 nm). The horizontal dips are BZ oscillations corresponding to the MoM lattice vector of 18.1 nm . **d-f**, R_{xx} as a function of n and B at field and charge carrier density at $-0.17\text{ V/nm} \leq D/\epsilon_0 \leq 0.17\text{ V/nm}$. No well-defined signatures of an additional Landau fan or BZ oscillations are seen near the CNP. **g-i**, Magnetic field and charge carrier density dependence of R_{xx} at $0.33\text{ V/nm} \leq D/\epsilon_0 \leq 0.66\text{ V/nm}$. An additional Landau fan starts at a MoM BI state at $n = (-1.1 \pm 0.2) \cdot 10^{12}\text{ cm}^{-2}$ corresponding to a different MoM length scale (with the estimated lattice vector of 19.8 nm consistent with the BZ oscillations) from that dominating in **a-c**.

S3. Temperature dependance of band insulator states

To demonstrate the existence of a finite band insulator gap, Δ_L , temperature dependence of longitudinal resistance, R_L , can be studied. At temperatures, $T > 10\text{K}$, the charge carriers across the band insulator gap are thermally activated resulting in a decreasing resistance at growing temperature (Fig. 4a, 5d). This is modeled by the Arrhenius law: $R_L \sim \exp\left(\frac{\Delta_L}{2k_B T}\right)$, where k_b is the Boltzmann constant. By fitting the resistance peak dependence on T (Fig. S4), the values of Δ_L can be extracted. Figures 4c, 5f in the main manuscript as well as Fig. S5a, b summarize the sizes of the band insulator gaps (Δ_L , diamonds) as a function of displacement field, D , comparing them

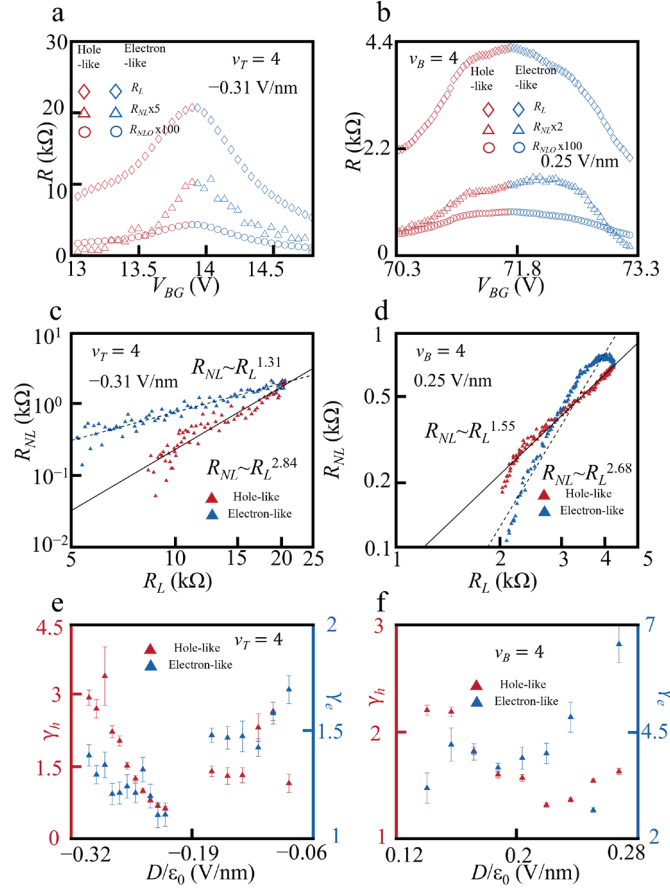


Figure S3 | Valley Hall effect at $\nu_T = 4$ and $\nu_B = 4$. **a, b**, Back gate voltage dependence of the local (R_L), non-local (R_{NL}) and non-local Ohmic resistance (R_{NLO}) near the $\nu_T = 4$ and $\nu_B = 4$ BI states at $D/\epsilon_0 = -0.31$ V/nm and $D/\epsilon_0 = 0.25$ V/nm respectively. The color highlights the types of carriers participating in electrical transport. **c, d**, The dependence of R_{NL} on R_L for hole-like (red) and electron-like (blue) carriers at $\nu_T = 4$ and $\nu_B = 4$ and the same D as in **a, b**. For each carrier type, the trendlines show a power law fit, $R_{NL} \sim R_L^\gamma$. **e, f**, The extracted power $\gamma = \gamma_h$ (γ_e) for hole- (electron-) like carriers as a function of displacement field at $\nu_T = 4$ and $\nu_B = 4$.

with the non-local gaps (Δ_{NL} , triangles) found from the thermal activation behavior of the non-local resistance, R_{NL} , as discussed in the main manuscript. The non-local gaps are consistently larger than the band insulator ones confirming the presence of a Berry curvature hot spot near the band edges. As the temperature increases, the charge carriers are thermally excited between the conduction and valence bands resulting in diminishing R_L . However, the larger Δ_{NL} compared to Δ_L , indicates that additional energy is needed to push the carriers away from the Berry curvature hot spot.

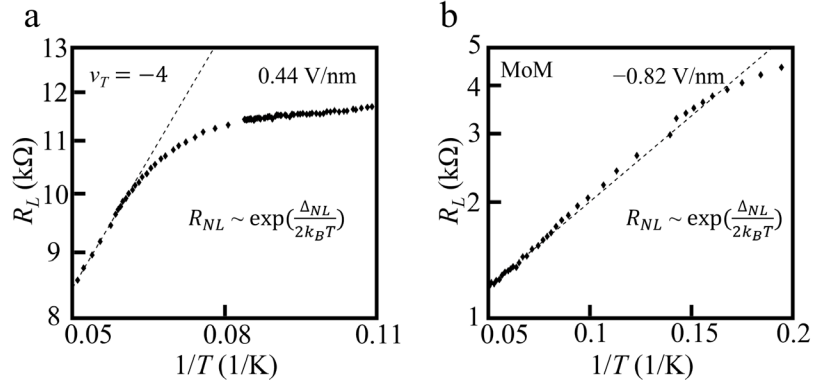


Figure S4 | Temperature dependence of local resistance of the $\nu_T = -4$ and MoM band insulator states. **a**, Local resistance peak of the $\nu_T = -4$ BI state as a function of inverse temperature, $1/T$, at $D/\epsilon_0 = 0.44$ V/nm. The dashed line indicates an Arrhenius fit of the resistance showing thermally activated behavior. **b**, Same as **a** but for the MoM BI state at $D/\epsilon_0 = -0.82$ V/nm.

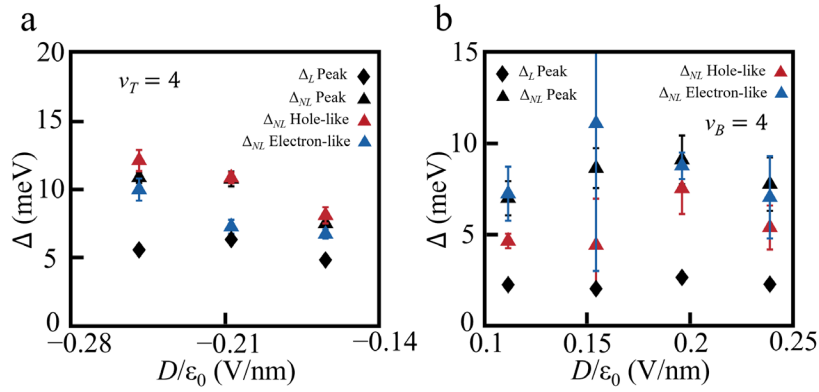


Figure S5 | Temperature dependence of the $\nu_T = 4$ and $\nu_B = 4$ band insulator states. **a**, **b**, Displacement field dependence of band insulator, Δ_L (diamonds), and non-local band gap, Δ_{NL} (triangles), found from Arrhenius fits of the $\nu_T = 4$ and $\nu_B = 4$ BI resistance peak (black) and half-peak (red and blue, with the colors corresponding to hole-like and electron-like carrier types).

S4. Results from a different region of the device

Inter-moiré, moiré-of-moiré Hofstadter butterflies and band insulator valley Hall effect were reproduced in a different region of the same device. The main manuscript discusses the measured local resistance in Region 1 between Contact 3 and Contact 4 of the device shown in Fig. 1b. Similarly, the longitudinal resistance, R_{xx} , between Contact 2 and Contact 3 corresponding to Region 2 of the same device can be measured. In this region, in addition to correlated insulator states at moiré half filling (Fig. S6a), displacement field tunable band-insulator states are observed at four charge carriers per top (bottom) moiré unit cell corresponding to twist angles of $1.48^\circ \pm 0.02^\circ$ ($1.66^\circ \pm 0.01^\circ$). At n in the range between full filling of the top and bottom moiré, inter-moiré Hofstadter butterflies (Fig. S6b, c) are observed with the BZ oscillations periodicity stemming from the MoM spatial periodicity with a lattice constant of 18.3 ± 0.1 nm. The same periodicity is

responsible for a moiré-of-moiré band insulator state observed at $n = -1.3 \cdot 10^{12} \text{ cm}^{-2}$ yielding a moiré-of-moiré Hofstadter butterfly (Fig. S6d) with the BZ oscillations' periodicity matching that in Fig. S6b, c.

By driving current, I_{73} , between Contact 7 and Contact 3 and measuring voltage, V_{82} , between Contact 8 and Contact 2 (Fig. S7a), a non-local resistance, $R_{NL} = V_{82}/I_{73}$, can be found as a function of D and n (Fig. S7b). Similar to Region 1, a finite non-local resistance is measured at $\nu_T = \pm 4$, $\nu_B = 4$, indicating the presence of Berry curvature hot spots. However, no signatures of R_{NL} are found in the MoM BI state, possibly indicating its high sensitivity to the exact twist angle

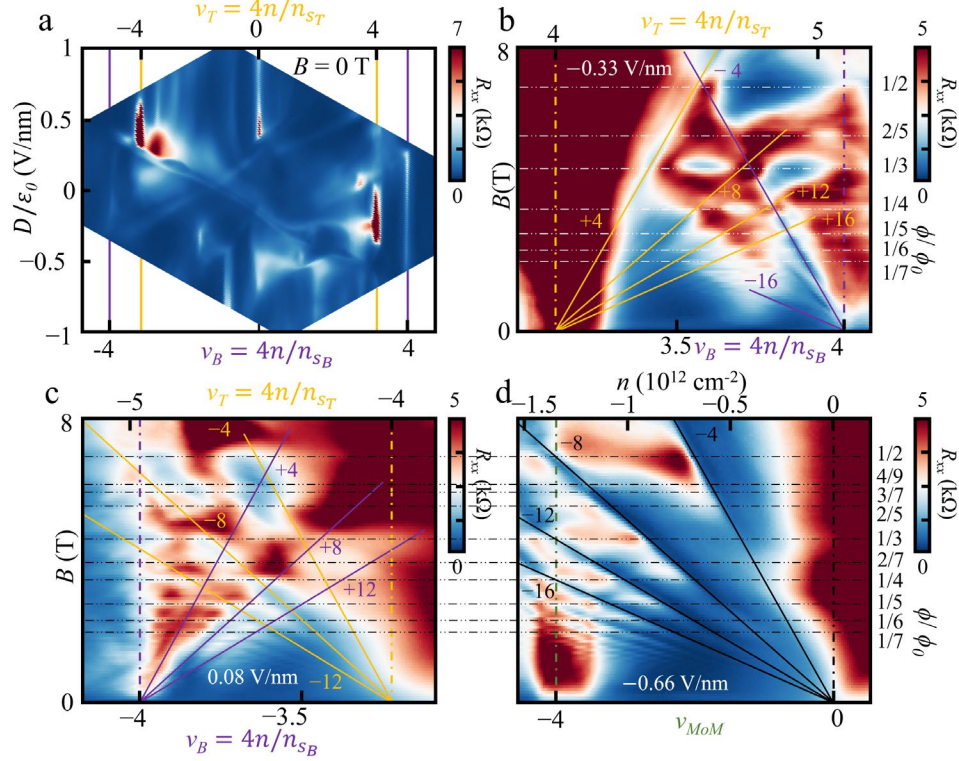


Figure S6 | Magneto-transport in Region 2 of the measured device. **a**, Longitudinal resistance, R_{xx} , between Contact 2 and Contact 3 as a function of charge carrier density, n , and displacement field, D . Resistance peaks of band-insulator states (highlighted by solid lines) at four charge carriers per top (yellow) and bottom (purple) moiré unit cell. **b**, R_{xx} as a function of the top (ν_T) and bottom (ν_B) moiré fillings and magnetic field. Inter-moiré Hofstadter butterfly at electron doping between overlapping Landau fans of the two moirés at $D/\epsilon_0 = -0.33 \text{ V/nm}$ is observed. SdH oscillations of the Landau fans are outlined by solid lines with the color referring to a single moiré. BZ oscillations at $\phi/\phi_0 = p/N$, with p, N being integers are traced by horizontal dash-dotted line. **c**, Same as **b** but at hole doping at $D/\epsilon_0 = 0.08 \text{ V/nm}$. **d**, Moiré-of-moiré Hofstadter butterfly originating from a moiré-of-moiré BI state at $-1.3 \cdot 10^{12} \text{ cm}^{-2}$ near the charge neutrality point at $D/\epsilon_0 = -0.66 \text{ V/nm}$. The BZ oscillations have the same periodicity as those in **b**, **c**.

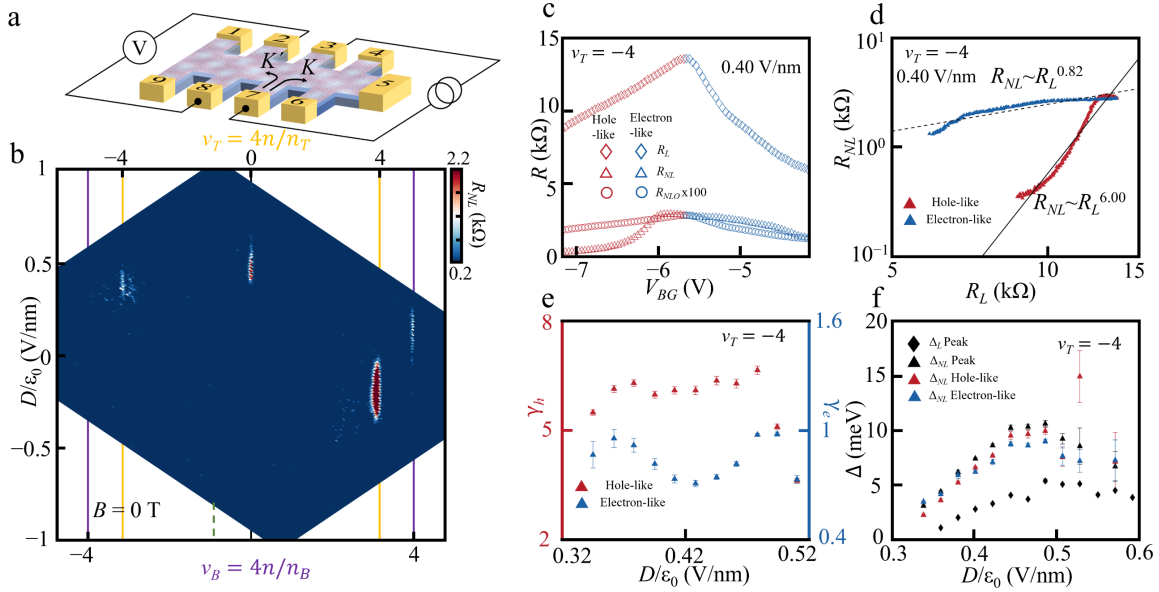


Figure S7 | Valley Hall effect in Region 2 of the tTBLG device. **a**, Measurement configuration for studying non-local transport in Region 2 of the tTBLG device. **b**, Non-local resistance, $R_{NL} = V_{82}/I_{73}$, found from the driven current and measured voltage in the configuration of **a** at varying D and n . The resistance peaks corresponding to the Berry curvature hot spots at $\nu_T = \pm 4$, $\nu_B = 4$ are reproduced in Region 2. **c**, Non-local (R_{NL}), local (R_L), and calculated non-local Ohmic resistance (R_{NLO}) contributing to non-local transport of the $\nu_T = -4$ BI at $D/\epsilon_0 = +0.40$ V/nm. **d**, R_{NL} as a function of R_L for hole-like (red) and electron-like (blue) carriers across the $\nu_T = -4$ BI band gap at $D/\epsilon_0 = +0.40$ V/nm. The dependence is consistent with power law fits for the hole-like (solid line) and electron-like (dashed line) carriers. **e**, Displacement field dependence of the powers extracted from the $R_{NL} \sim R_L^{\gamma_h}$ ($R_{NL} \sim R_L^{\gamma_e}$) fits for the hole- (electron-) like charge carriers. **f**, Estimated from the Arrhenius fits, the local, Δ_L , non-local, Δ_{NL} , bandgaps at the BI peak (black) and half-peak (blue and red, corresponding to the electron- and hole-like carriers) value of the resistance as a function of D .

configuration determining the atomic lattice reconstruction landscape. Near $\nu_T = -4$, the measured R_{NL} (Fig. S7c) is two orders of magnitude larger than the trivial Ohmic resistance from the stray charge currents. This points to the presence of a transverse valley current responsible for the increased non-local resistance. The plotted R_{NL} as a function of R_L (Fig. S7d) reveals two separate non-linear power law dependences, $R_{NL} \sim R_L^\gamma$, characteristic to a valley Hall effect, for the hole-like ($\gamma = \gamma_h$) and electron-like ($\gamma = \gamma_e$) charge carrier types changing across the $\nu_T = -4$ insulator bandgap. Changing D has no consistent effect on the form of the power law dependence (Fig. S7e). However, over the entire range of the displacement field, both powers differ from $\gamma = 1$ excluding the possibility of trivial Ohmic transport. Found from the resistance behavior during thermal activation, the non-local bandgap, Δ_{NL} , turns out to be higher than Δ_L over the entire range of

displacement fields at which the non-local signal exists (Fig. S7f). This is consistent with the Berry curvature hot spot model depicted in Fig. 4d.

The main experimental observations of inter-moiré butterflies, MoM band-insulator states and atomically enhanced Berry curvature have all been reproduced in different device region, suggesting the robustness of the observed emergent quantum phenomena. The differences in quantitative details (ie., the extracted power law dependence) further supports that the Berry curvature of reconstructed bands are extremely sensitive to microscopic details of reconstructed local atomic landscape, which can realistically vary with the presence of even slight twist-angle inhomogeneity.

S5. Decay length of valley currents

To confirm the origin of the non-local signal to be due to the presence of Berry curvature hot spots, we investigate how R_{NL} depends on L , the distance between the driven current and the non-local voltage probes (Fig. S8a). In this configuration, at an electric field, E , driving the charge current, the Berry curvature hot spot yields a non-zero transverse valley current (valley Hall effect), $J_v = \sigma_{xy}^v E$. At a band-insulator state, the transverse valley Hall conductivity, σ_{xy}^v , is expected to be $M \cdot e^2/h$, where M is the total Berry flux of the occupied states below the Fermi energy. Subsequently, the inverse valley Hall effect is responsible for generating the non-local signal, R_{NL} , decaying with L (Fig S8, b and c). Following the previously established methods¹⁻⁴, we fit the length dependence of R_{NL} at the $\nu_T = -4$ (Fig. S8b) and MoM (Fig. S8c) BI states with the model expression

$$R_{NL} = \left(\frac{w}{2\xi}\right) (\sigma_{xy}^v)^2 \rho_{xx}^3 \exp(-L/\xi), \quad (\text{S1})$$

where w is the width of the valley channel, ξ is the valley decay length, and ρ_{xx} is the longitudinal resistivity. For $\nu_T = -4$ and MoM BI we found ξ to be $4 \pm 2 \mu\text{m}$ and $2.0 \pm 0.1 \mu\text{m}$ respectively, consistent with the expected inter-valley scattering lengths. Due to a larger spatial periodicity, MoM is more vulnerable to angle inhomogeneity which explains the smaller decay length. For both BI states, σ_{xy}^v is found to be $\sim 3e^2/h$ confirming the Berry curvature hot spot being the origin of the non-local signal.

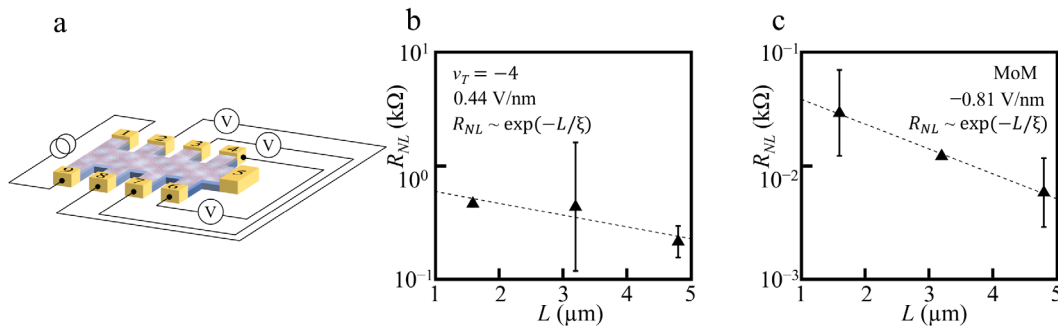


Figure S8 | Decay length of the non-local signal. **a**, Non-local transport measurement configuration with non-local voltages simultaneously measured at different distances from the driven current. **b**, **c**, R_{NL} calculated from the measured non-local voltages as a function of L , the distance from the driven current, at $\nu_T = -4$ ($D/\epsilon_0 = +0.44 \text{ V/nm}$) and MoM ($D/\epsilon_0 = -0.81 \text{ V/nm}$) BI states. The dashed lines represent data fits with equation S1.

S6. Calculation of the electronic structure

To obtain the electronic structure of tTBLG, we follow the momentum-space model in⁵ with modified hopping parameters. The Hamiltonian in momentum space can then be formally written as

$$H_K(\mathbf{q}) = \begin{bmatrix} H^1(\mathbf{q}) + \delta_1 \mathbb{I}_{2 \times 2} & T^{12} & 0 \\ T^{12\dagger} & H^2(\mathbf{q}) + \delta_2 \mathbb{I}_{2 \times 2} & T^{23} \\ 0 & T^{23\dagger} & H^3(\mathbf{q}) + \delta_3 \mathbb{I}_{2 \times 2} \end{bmatrix}. \quad (\text{S2})$$

The diagonal blocks describe the low-energy Hamiltonian of the Bernal bilayer graphene with δ_ℓ representing the onsite potential due to the applied vertical displacement field. The intralayer parameters are taken from⁶. The off-diagonal terms describe the interlayer interaction between adjacent Bernal bilayers. More explicitly, the intralayer terms in the (A_1, B_1, A_2, B_2) basis can be expressed as:

$$H^\ell(\mathbf{q}) = \begin{bmatrix} H_D^{\ell,t}(\mathbf{q}) & g^\dagger(\mathbf{q}) \\ g(\mathbf{q}) & H_D^{\ell,b}(\mathbf{q}) \end{bmatrix}, \quad (\text{S3})$$

where the superscript t/b denotes the top and bottom Bernal bilayer graphene. H_D is the rotated Dirac Hamiltonian for monolayer graphene.

$$H^{\ell,t/b}(\mathbf{q}) = \begin{bmatrix} \Delta_{t/b} & \hbar v_F e^{i\theta_\ell} q_+ \\ \hbar v_F e^{i\theta_\ell} q_- & \Delta_b \end{bmatrix}, \quad (\text{S4})$$

where $\theta_1 = \theta_{12}$, $\theta_2 = 0$, and $\theta_3 = \theta_{23}$, and $v_F = 0.8 \times 10^6$ m/s is the monolayer graphene Fermi velocity, $q_\pm = q_x \pm q_y$. The diagonal $\Delta_{t/b}$ represents the on-site potential of dimer sites with respect to nondimer sites, and $\Delta_{t/b} = 0.050$ eV if the neighboring layer is not vacuum and 0 otherwise. $g(\mathbf{k})$ is the parabolic part of the band structure:

$$g(\mathbf{q}) = \begin{bmatrix} \hbar v_4 q_+ & \gamma_1 \\ \hbar v_3 q_- & \hbar v_4 k_+ \end{bmatrix}, \quad (\text{S5})$$

where $\gamma_1 = 0.4$ eV is the hopping between dimer sites, $\gamma_3 = 0.32$ eV, $\gamma_4 = 0.044$ eV and $v_i = \frac{\sqrt{3}\gamma_i a}{2\hbar}$ where a is the monolayer graphene lattice constant.

For the interlayer coupling, we keep the nearest neighbor coupling in momentum space

$$T_{\alpha\beta}^{ij}(\mathbf{q}^{(i)}, \mathbf{q}^{(j)}) = \sum_{n=1}^3 T_{\alpha\beta}^{q_n^{ij}} \delta_{\mathbf{q}^{(i)} - \mathbf{q}^{(j)}, -\mathbf{q}_n^{ij}}, \quad (\text{S6})$$

where $\mathbf{q}_1^{ij} = K_{L_i} - K_{L_j}$, $\mathbf{q}_2^{ij} = \mathcal{R}^{-1}\left(\frac{2\pi}{3}\right)\mathbf{q}_1^{ij}$, $\mathbf{q}_3^{ij} = \mathcal{R}\left(\frac{2\pi}{3}\right)\mathbf{q}_1^{ij}$ and $\mathcal{R}(\theta)$ is the counterclockwise rotation matrix by θ . We take into account the out-of-plane relaxation by letting $t_{AA}^{ij} = t_{BB}^{ij} = \omega_0 = 0.07$ eV and $t_{AB}^{ij} = t_{BA}^{ij} = \omega_1 = 0.11$ eV due to the strengthened interaction between AB/BA sites from relaxation.

$$T^{q_1^{ij}} = \begin{bmatrix} \omega_0 & \omega_1 \\ \omega_1 & \omega_0 \end{bmatrix}, T^{q_2^{ij}} = \begin{bmatrix} \omega_0 & \omega_1 \bar{\phi} \\ \omega_1 \phi & \omega_0 \end{bmatrix}, T^{q_3^{ij}} = \begin{bmatrix} \omega_0 & \omega_1 \phi \\ \omega_1 \bar{\phi} & \omega_0 \end{bmatrix}, \quad (\text{S7})$$

where $\phi = e^{\frac{i2\pi}{3}}$ and $\bar{\phi} = e^{-\frac{i2\pi}{3}}$.

S7. Calculation of the atomic relaxation pattern

We follow the model in⁷ for the relaxation pattern model and refer to the reference for details of the model. We modify the parameters of the model to reflect the twisted triple-bilayer graphene system. We take the Bernal bilayer graphene shear and bulk moduli $G = 94704$ meV/unit cell, $K = 139036$ meV/unit cell, twice that of the monolayer graphene. For the interlayer coupling, we obtain the generalized stacking fault energy coefficients to be $c_0 = 14.508$ meV/cell, $c_1 = 6.841$ meV/cell, $c_2 = -0.679$ meV/cell, $c_3 = -0.153$ meV/cell, $c_4 = 0.493$ meV/cell, and $c_5 = 0.0313$ meV/cell⁸. We obtained these values by performing 9x9 uniformly shifted first-principles density functional theory calculations with the Vienna Ab initio Simulation Package (VASP)⁹⁻¹¹. The van der Waals force is implemented through the vdW-DFT method using the SCAN+rVV10 function

REFERENCES

1. Gorbachev, R. V. *et al.* Detecting topological currents in graphene superlattices. *Science* **346**, 448–451 (2014).
2. Shimazaki, Y. *et al.* Generation and detection of pure valley current by electrically induced Berry curvature in bilayer graphene. *Nature Phys* **11**, 1032–1036 (2015).
3. Sinha, S. *et al.* Bulk valley transport and Berry curvature spreading at the edge of flat bands. *Nat Commun* **11**, 5548 (2020).
4. Li, Y., Amado, M., Hyart, T., Mazur, G. P. & Robinson, J. W. A. Topological valley currents via ballistic edge modes in graphene superlattices near the primary Dirac point. *Commun Phys* **3**, 1–7 (2020).
5. Zhu, Z., Carr, S., Massatt, D., Luskin, M. & Kaxiras, E. Twisted Trilayer Graphene: A Precisely Tunable Platform for Correlated Electrons. *Phys. Rev. Lett.* **125**, 116404 (2020).
6. Koshino, M. Band structure and topological properties of twisted double bilayer graphene. *Phys. Rev. B* **99**, 235406 (2019).
7. Zhu, Z., Cazeaux, P., Luskin, M. & Kaxiras, E. Modeling mechanical relaxation in incommensurate trilayer van der Waals heterostructures. *Phys. Rev. B* **101**, 224107 (2020).
8. Carr, S. *et al.* Relaxation and domain formation in incommensurate two-dimensional heterostructures. *Phys. Rev. B* **98**, 224102 (2018).

9. Kresse, G. & Hafner, J. Ab initio molecular dynamics for liquid metals. *Phys. Rev. B* **47**, 558–561 (1993).
10. Kresse, G. & Furthmüller, J. Efficiency of ab-initio total energy calculations for metals and semiconductors using a plane-wave basis set. *Computational Materials Science* **6**, 15–50 (1996).
11. Kresse, G. & Furthmüller, J. Efficient iterative schemes for ab initio total-energy calculations using a plane-wave basis set. *Phys. Rev. B* **54**, 11169–11186 (1996).